Journal of Power Sources 196 (2011) 9654–9664

Contents lists available at ScienceDirect

Journal of Power Sources

journal homepage: www.elsevier.com/locate/jpowsour

Effect of electrolyte transport properties and variations in the morphological parameters on the variation of side reaction rate across the anode electrode and the aging of lithium ion batteries

H. Jannesari[a,b,*], M.D. Emami[a], C. Ziegler[b]

[a] Department of Mechanical Engineering, Isfahan University of Technology, 84156-83111 Isfahan, Iran
[b] Laboratory for MEMS Applications, Department of Microsystems Engineering – IMTEK, University of Freiburg, Georges-Köhler-Allee 106, 79110 Freiburg, Germany

ARTICLE INFO

Article history:
Received 22 April 2011
Received in revised form 7 July 2011
Accepted 7 July 2011
Available online 19 July 2011

Keywords:
Solid electrolyte interface
Morphology
Nanomaterials
Ionic conductivity
Variation
Aging

ABSTRACT

In this work, for the first time, we model the variation of solid electrolyte interface (SEI) across the depth of anode electrode of lithium ion battery. It is anticipated that due to higher thickness of SEI layer at the electrode side connected to the separator, a more critical condition prevails there. The present work also investigates the effects of *variations* in the morphological parameters including porosity, interfacial surface area and active particle radius across anode electrode on the uniformity of side reaction. Moreover, the sensitivity of the side reaction uniformity to electrolyte parameters, such as diffusion and ionic conductivity, is studied. Results show that the ionic conductivity has a major role on the uniformity, and could reduce critical conditions in the part of electrode next to the separator. Moreover, simulation results show that increasing ionic conductivity could significantly prolong the lifetime of the battery. An increase in electrolyte diffusion improves side reaction uniformity. Results also show that positive gradients of morphological parameters across anode electrode, when parameters are changed independently, have considerable effects on uniformity of side reaction. This could be a criterion in choosing new morphologies for the part of anode electrode connected to separator.

1. Introduction

During the last five decades researchers have developed different theoretical models to predict the performance of batteries [1–3]. An outcome of these efforts is a set of general mathematical equations for the lithium ion battery. This set includes concentrated solution theory, porous media theory, Ohm's laws in heterogeneous media, Butler–Volmer kinetics and various balance laws [4].

Moreover, there have been studies on modeling aging mechanisms and life prediction of lithium ion batteries. Darling and Newman modeled the side reaction in the positive electrode of manganese lithium ion battery assuming Tafel kinetics [5]. However, they neglected the variation of electrolyte concentration due to the side reaction. Christensen and Newman studied the effect of lithium consumption and increase of solid electrolyte thickness on the capacity and rate capability of the cell [6]. They also studied different methods for compensating lithium ion loss and their impact on the charge density of the battery [7]. Yoshida et al. studied degradation mechanism and life prediction of lithium ion battery during storage in different temperatures [8]. They measured the thickness of the SEI layer on the anode active material using focused ion beam, scanning electron microscope, and X-ray photoelectron spectroscopy.

Ramadass et al. studied the performance of commercial $LiCoO_2$ and spinel-based Li-ion cells during cycling [9]. Then they presented a capacity fade model for lithium ion cells [10,11]. The authors considered the effect of constant current (CC) and constant voltage (CV) charging regimes, end of charge voltage, depth of discharge, film resistance, and the exchange current density on the capacity change and battery performance. However, they have neglected the effect of transport of lithium in the electrolyte phase. Ning et al. investigated the capacity fade of lithium ion batteries cycled at high discharge rates [12]. In another work, Ning et al. modeled the effect of lithium ion consumption and the increase in resistance during SEI formation on the aging of lithium ion batteries [13]. They considered the effect of lithium transport in the electrolyte phase, but assumed a uniform SEI thickness across the anode electrode during cycling.

Side reactions and nonisothermal effects were modeled for Nickel Metal-Hydride batteries in Ref. [14] by Albertus et al. They considered material balance equations including source term expressions for production and consumption of materials in side

* Corresponding author at: Department of Mechanical Engineering, Isfahan University of Technology, 84156-83111 Isfahan, Iran. Tel.: +98 311 772 0523; fax: +98 311 391 2628.
E-mail address: hjannesari@me.iut.ac.ir (H. Jannesari).

0378-7753/$ – see front matter © 2011 Elsevier B.V. All rights reserved.
doi:10.1016/j.jpowsour.2011.07.026

Nomenclature

a	specific interfacial area of solid phase particles per unit volume of porous electrode ($m^2\ m^{-3}$)
c_e	concentration of electrolyte ($mol\ m^{-3}$)
$c_{e,0}$	initial concentration of electrolyte ($mol\ m^{-3}$)
c_t	maximum concentration of Li in the solid phase ($mol\ m^{-3}$)
c_s	concentration of Li inside an electrode particle ($mol\ m^{-3}$)
i_1	current density at particle–electrolyte interface ($A\ m^{-2}$)
i_2	current density in solution ($A\ m^{-2}$)
I	applied current density ($A\ m^{-2}$)
Φ_1	solid potential (V)
Φ_2	electrolyte potential (V)
U	open circuit potential (V)
U_{para}	parasitic equilibrium potential (V)
j	reaction rate per unit area ($mol\ m^{-2}\ s^{-1}$)
i_0	exchange current density ($A\ m^{-2}$)
j_{para}	parasitic reaction rate per unit area ($mol\ m^{-2}\ s^{-1}$)
$j_{0,para}$	parasitic rate constant ($mol\ m^{-2}\ s^{-1}$)
t	time (s)
r	radius (m)
R_a, R_c	active particles radius of anode and cathode electrodes (m)
F	Faraday constant ($C\ mol^{-1}$)
k_e	ionic conductivity of electrolyte ($S\ m^{-1}$)
k	effective ionic conductivity of electrolyte ($S\ m^{-1}$)
D	effective diffusion coefficient of electrolyte ($m^2\ s^{-1}$)
D_e	diffusion coefficient of electrolyte ($m^2\ s^{-1}$)
D_s	intercalated diffusion coefficient ($m^2\ s^{-1}$)
$f_\pm$	mean molar activity coefficient
α_a	anodic transfer coefficients
α_c	cathodic transfer coefficients
R	gas constant ($J\ mol^{-1}\ K^{-1}$)
T	temperature (K)
k_f	SEI film conductivity ($S\ m^{-1}$)
σ_s	solid conductivity ($S\ m^{-1}$)
ε	volume fraction of electrolyte in electrode
ε_{fl}	volume fraction of filler materials
t_0^+	positive ion transfer number
z_+	charge of cation in the electrode reaction
ν_+	number of cations into which a mole of electrolyte dissociates
s_+	stoichiometric coefficient of cations involved in the general insertion process
n	number of electrons transferred in the electrode reaction
M	molecular weight ($kg\ mol^{-1}$)
ρ_f	film density ($kg\ m^{-3}$)
δ_f	film thickness (m)
R_f	film resistance ($\Omega\ m^2$)
$R_{f,0}$	initial film resistance ($\Omega\ m^2$)
CSX	average value of the lithium stoichiometry in the anode electrode
L_a	anode electrode thickness (m)

reactions and the corresponding terms in the charge conservation equation. They simulated over-potential protection, self-discharge and pressure–voltage–temperature coupling. However, they did not report results for large numbers of cycling.

Morphological parameters constitute a very important category of parameters that appear in the model equations. This includes the porosity of the electrodes, the interfacial surface area, and the particle radius of active materials in the electrode. Broussely et al. studied the effect of side reaction on aging of lithium ion batteries, either on rest or on cycling [15,16]. It is stated that progressive clogging of the micro-pores of the negative electrode by passivation layer growth could reduce the active surface area significantly. This points to the importance of negative/anode electrode porosity in controlling the capacity fade under charge cycling. The effect of cathode electrode with two characteristic particle size distributions on the performance of lithium ion battery was investigated by Darling and Newman [17]. Their results show that the effect of particle size distribution is more important for the open circuit condition than for the cell voltage under galvanostatic operation.

Despite the large amount of publication in this area in all the aforementioned references the morphological parameters are considered to be uniform in space across the electrodes. However, recent developments especially in the field of nanomaterials and nanotechnology have provided better control of the morphology of the active materials during the production process [18–20]. As a result, it is logical to consider the change of the material morphology across the electrodes in theoretical models. This is especially important in the case of high energy cells with thicker electrodes where morphological parameters are very likely to change across the depth of electrode during cycling.

Christensen mentioned that in most cases, non-uniform operation conditions prevail across the electrodes in commercial lithium ion batteries [21]. Additionally, the reaction rates at the interfaces between electrodes and separator are higher than in other regions, which might cause more critical condition in this section of the battery. A further evidence for non-uniform operation conditions in the electrode layers are the results of direct in situ observation of lithium transport. In Ref. [22] the variation of reaction rate across the negative electrode is shown.

Given this situation, the present paper focuses on the improvement of the predictive capabilities of common lithium ion battery models with respect to non-uniformity of material properties. For the first time, the focus is put on studying how solid electrolyte interface, parasitic side reaction rate and resistance vary across anode electrode. It is also of interest to investigate changes in the uniformity of aforementioned parameters across the anode to the *variation* of morphological characteristics including porosity, interfacial surface area and active particle radius across anode electrode and electrolyte parameters including Li-diffusion and ionic conductivity.

2. Computational domain and experimental setup

A schematic model of the lithium ion battery and its associated coordinate system are shown in Fig. 1. The domain represents a cross section perpendicular to the membrane. The computational domain is divided into different subdomains R_i that describe the current collectors R_1 and R_5, the electrodes R_2 and R_4, and the separator R_3. The sub-domains are coupled with each other via appropriate boundary conditions at the boundaries denoted by $B_{i,j}$.

For model validation, the simulation results are compared with experimental data of Ref. [13]. Therein the experimental setup comprises a lithium ion battery with Li_xCoO_2 cathode, mesocarbon micro beads (MCMB) anode and 1 M $LiPF_6$ in a mixture of EC:PC:EMC:DEC (30:5:35:30). The battery is cycled at a charge rate of 1 C and a discharge rate of 0.5 C for 1968 cycles. End of charge voltage (EOCV) in charge mode is 4 V and cut off current at the end of CV part of charge is 50 mA.

To account for the variation of morphological parameters during cycling, as well as verifying the corresponding assumptions in the modeling part, we tested a 2.2 Ah commercial lithium ion

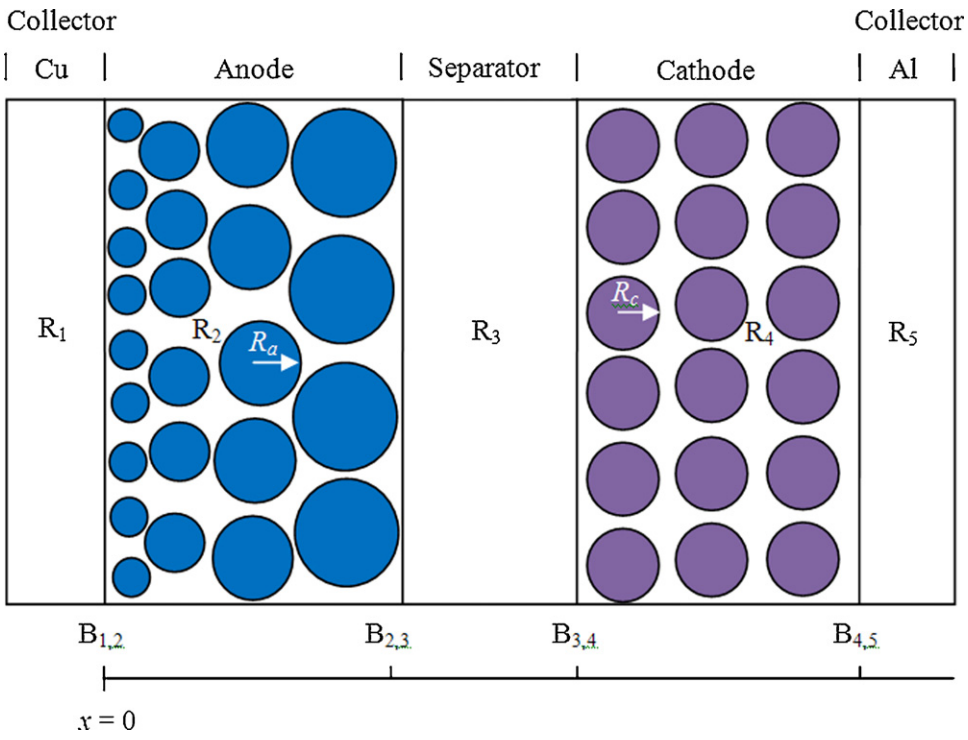

Fig. 1. schematic diagram of the lithium ion battery model and used coordinate system.

battery (18650 Varta) with $LiCoO_2$|methyl ethyl carbonate, ethylene carbonate carbon configuration. The battery is connected to an AkkuMaster C5 electrochemical interface in order to control charge and discharge rates to 1 C. End of charge voltage is 4.2 V, End of discharge voltage is 2.9 V and cut off current at the end of CV part of charge is 440 mA.

The battery is cycled for 1267 times. It is discharged before opening in an Argon filled glove box which inhibits undesired reactions during opening the battery. Anode, cathode and separator parts are separated in glove box and stored in gastight containers before transfering to SEM and FIB/SEM imaging. The sample is investigated with an FEI Quanta three-dimensional dual-beam FIB/SEM instrument. The first step is preliminary screening of the electrode layer to identify a suitable position for FIB/SEM investigation where a cavity was produced by the ion beam. The FIB consisted of Ga^+ ions which were accelerated with a voltage of 30 kV. This was followed by SEM imaging of the exposed surface.

3. Model description

The governing equations describing the cycling behavior of a lithium ion battery should take several highly coupled physical and chemical phenomena into account. A detailed description of the following transport phenomena is provided in this paper:

1. The dynamic transport of lithium ions through the electrolyte in electrodes porous media and separator.
2. The time-dependent diffusion of lithium ions through the solid active particles of the electrodes.
3. Conduction of electrons through the solid parts of anode and cathode.
4. Ionic charge transport through the electrolyte.

The dynamics of system stems from dependency of material transport, through the electrolyte and the solid active particles, to the time derivatives of c_e and c_s, respectively. This means, the charge transports intrinsically follows the other effects and depends on time due to the coupling phenomena.

The transport model is described in the framework of porous media theory.

The electrolyte transport is described in the framework of concentrated solution theory. The charge transfer is modeled by combination of Ohm's law and charge conservation. The Butler–Volmer kinetics is assumed for the electrochemical reactions at anode and cathode side. The Tafel kinetics is considered for the electrochemical side reaction.

The lithium ion battery is a complex system involving both microscopic and macroscopic geometric features, coupled transport processes, and the electrochemical reaction. The main assumptions used in this model are as follows:

1. The model is one-dimensional and isothermal.
2. Only solid and liquid are considered, the gas phase and its pressure inside the cell are neglected.
3. All active particles are smooth spheres and are in contact with the electrolyte molecules.
4. The electrolyte is binary and electro-neutral.
5. The electrolyte conductivity and diffusivity vary with concentration.
6. The effects of porosity and tortuosity on the electrolytic transport properties are considered based on Bruggeman exponents.
7. SEI growth is considered on anode side only.
8. Aging is due to the consumption of lithium ions and precipitating side reaction products over the surface of the anode particles.
9. The dominant side reaction at the anode electrode is two electron reduction of ethylene carbonate at the anode/electrolyte interface during charge process [13].

Fig. 2 shows scanning electron microscopy (SEM) images of anode (a and b) and cathode surface (c and d) of the sample battery after the first and the 1267th charge cycling. From these images it is evident that size distribution, particle and surface

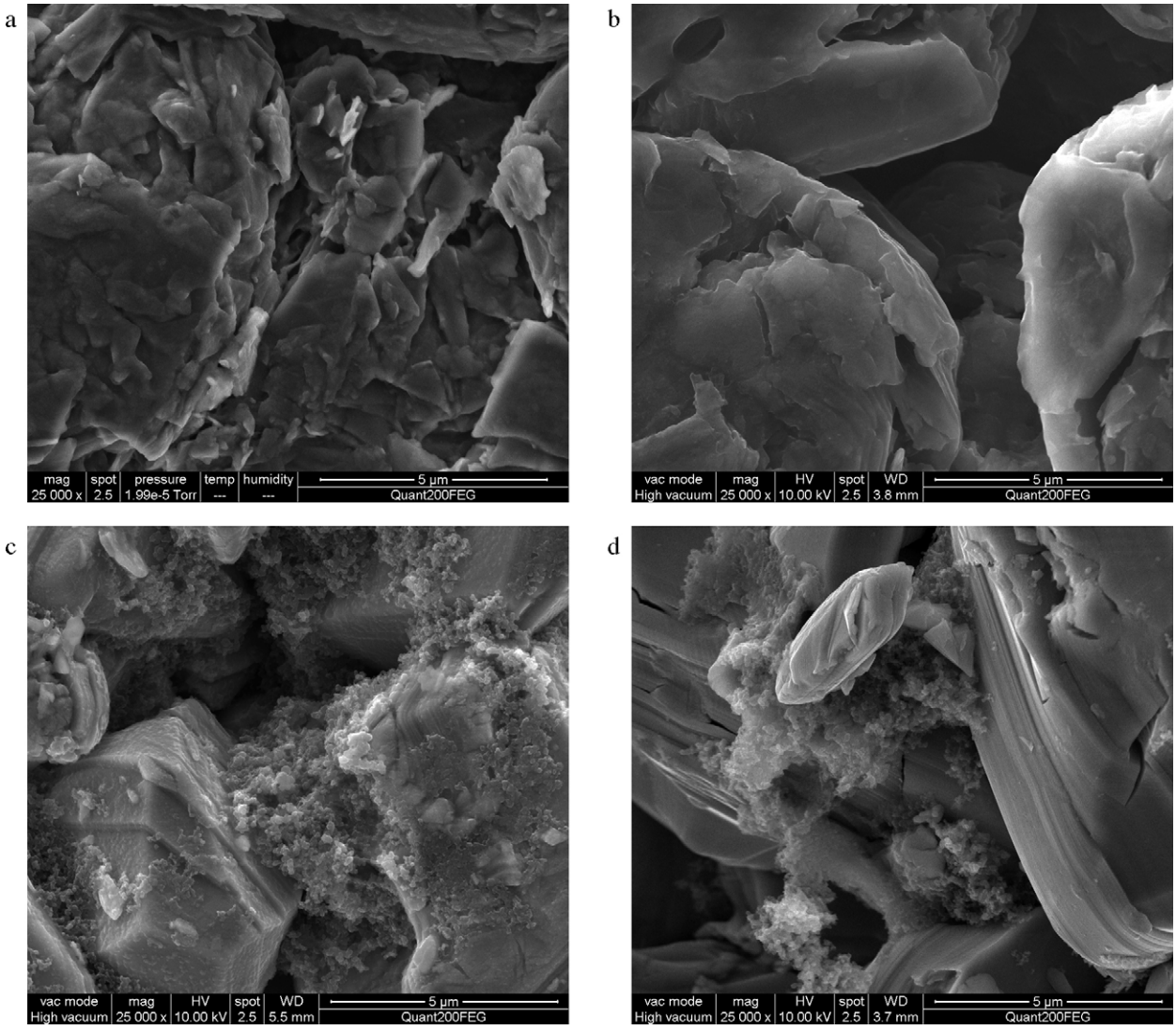

Fig. 2. SEM graph of anode (a and b) and cathode (c and d). (a and c) graphs of a fresh cell while (b and d) graphs of a cell after 1267 electrochemical cycling.

morphology, phase contact area and electrolyte wetting properties will have strong impact on the performance of the electrodes. Correspondingly to assume all particles as smooth spheres is one of the strongest assumptions that is clearly driven by the feasibility of the model.

Porous media theory, however, shows that a microscopic random porous medium – such as an electrode – can be modeled by a macro-homogeneous isotropic layer such as a layer of suitably chosen spheres [23].

The porosity and tortuosity that are indicated on the surface SEMs (Fig. 2), and clearly shown on the FIB/SEM image of the cathode after 1267 electrochemical cycling (Fig. 3), are taken into account. Therefore, one of the most important features of these materials is captured by the model. Additionally, these figures show that there is virtually no change in porosity during cycling. Consequently, porosity may be assumed constant with respect to time in the numerical solution procedure. While for the anode side Ref. [8] shows that a significant SEI layer formation on the anode side can be expected, no such indication is found in the FIB/SEM images of the cathode; thus experimentally underlining model assumption number 7.

There are two main features that distinguish the present work from others. In this work for the first time the effects of variation

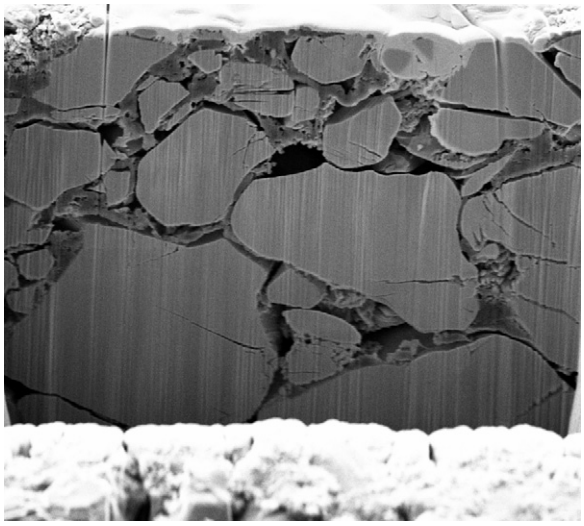

Fig. 3. the FIB/SEM image of the cathode after 1267 electrochemical cycling.

of porosity, specific interfacial area and radius of active particles across anode electrode have been studied. Moreover, the assumption of constant solid electrolyte interface thickness and resistance has been relaxed in the current work.

4. Model equations and parameters

Table 1 shows the governing transport equations and the supporting equations. Eq. (1) represents material balance of the electrolyte. This equation relates the time change of electrolyte concentration, c_e, to the electrochemical reaction rate per unit area, j and the flux of lithium ions. The flux of lithium ions is a function of the concentration gradient and the electric field whereas the source/sink term depends on the production/consumption rates of the governing electrochemical reaction which are equal to zero in separator region, R_3. Porosity, ε, and interfacial surface area, a, are functions of position, x, across anode electrode. Eq. (2) represents the Li material balance in the solid phase which is based on Fick's second law. Eqs. (3) and (4) are the Ohm's laws, respectively, for the solid (electrons) and electrolyte (lithium ions) phases, respectively. In addition to the ion migration that is driven by the potential gradient, $\nabla\Phi_2$, the diffusion potential is included in Eq. (4).

Following Ref. [24], the ionic conductivity, k, is considered a function of ionic concentration, c_e. The mean activity coefficient, $f_\pm$, is set constant in the pressure and temperature working range. Eq. (5) describes the conservation of the current which is a result of electro-neutrality. Faraday's law, Eq. (6), explains the relation between ionic current, i_2, and Li material production rate, j. The kinetic of the governing electrochemical reactions is described using the Butler–Volmer equation, Eq. (7). This equation is used in the cathode and the anode subdomains. Eq. (8) purposes an expression for calculating exchange current density, i_0, which is a function of Li concentration in electrode and electrolyte. The Tafel equation, Eq. (9), is used for calculating parasitic pore wall flux, j_{para}, in the anode electrode. Here it is assumed that the electrochemical side reaction is irreversible. The effective values of the effective electrolytic diffusivity, D, are described by Bruggeman exponents in Eq. (10) to take the porous structure of anode, cathode and separator into account.

Eqs. (11)–(13) contain the aging mechanisms of parasitic side reaction. The film thickness, δ_f, is obtained by calculating volume of side reaction products which cover the surface of anode active particles. Moreover, for obtaining the film resistance of anode electrode, R_f, a linear relation between film resistance and thickness is assumed. In the cathode subdomain R_4, the film resistance, R_f, is zero. Finally Eq. (13) calculates the average of lithium stoichiometry loss across the anode electrode, CSX.

There is a wide discrepancy in transport model parameters in literature. The reason for this situation is experimental uncertainty, differences in electrode microstructure, different states of charge, and differences in measurement techniques [17,25,26]. The required parameters used in this work are listed in Table 2. Most of them are identical to those used in Ref. [13]. However, here the ionic conductivity, k, is considered a function of electrolyte concentration c_e [24],

$$k(c_e) = 10^{-4} + 177.9\times10^{-5}c_e^{1.093}\varepsilon^{1.5} \times e^{-1.2754\left(-0.857+8.305\times10^{-4}c_e\right)+0.04\left(-0.857+8.305\times10^{-4}c_e\right)^2} \quad (14)$$

In Ref. [13] it is mentioned that modeling parameters are based on information in [1,10] but there are some discrepancies among these data. For example the value for the electrolyte diffusion is different. However, the extent of accuracies of these values is adequate for a semi-quantitative study in the present work.

Table 1
Governing equations.

Explanation	Equation		Initial and boundary condition
Material balance in the solutes	$\varepsilon(x)\frac{\partial c_e(x)}{\partial t} = \nabla\cdot(\varepsilon(x)D(c_e(x))\nabla c_e(x)) - \frac{i_2(x)\cdot\nabla t_+^0(c_e(x))}{z_+\nu_+F} + \frac{a(x)j(x)(1-t_+^0)}{\nu_+}$	(1)	$c_e = c_{0,e}$ at $t=0$ $\nabla c_e = 0$ at $B_{1,2}$ and $B_{4,5}$
Material balance in the solid phase	$\frac{\partial c_s(x)}{\partial t} = D_s\left[\frac{\partial^2 c_s(x)}{\partial r^2} + \frac{2}{r(x)}\frac{\partial c_s(x)}{\partial r}\right]$	(2)	$c_s = c_{0,e}$ at $t=0$ $j_n = -D_s\frac{\partial c_s}{\partial r}$ at $r = R_a$ or R_c
The Ohm's law in the matrix	$i_1(x) = -\sigma_s\nabla\Phi_1(x)$	(3)	$\nabla\Phi_1 = -I/\sigma$ at $B_{1,2}$ and $B_{4,5}$ (CC) $\Phi_1(B_{1,2}) - \Phi_1(B_{1,2}) = \text{EOCV}$ (CV)
The Ohm's law in the electrolyte	$\nabla\Phi_2(x) = -\frac{i_2(x)}{k(c_e(x))} - \frac{RT}{F}\left(1+\frac{\partial\ln f_\pm}{\partial\ln c_e(x)}\right)\left(\frac{s_+}{n\nu_+} + \frac{t^0(c_e(x))}{z_+\nu_+}\right)\nabla\ln c_e(x)$	(4)	$\Phi_1 = 0$ at $B_{4,5}$
Conservation of current	$I = i_1(x) + i_2(x)$	(5)	–
Faraday's law	$a(x)j(x) = -\frac{s_i}{nF}\nabla\cdot i_2(x)$	(6)	$i_2 = I$ between $B_{2,3}$ and $B_{3,4}$
Kinetic expression (Butler–Volmer equation)	$\nabla i_2(x) = a(x)i_0\left[\exp\left(\frac{\alpha_a F(\Phi_1(x)-\Phi_2(x)-U-Fij(x)R_f(x))}{RT}\right) - \exp\left(\frac{-\alpha_c F(\Phi_1(x)-\Phi_2(x)-U-Fij(x)R_f(x))}{RT}\right)\right]$	(7)	–
Exchange current density measurement	$i_0 = i_0'c_e^{\alpha_a}(c_{\max}-c_s)^{\gamma\alpha_a}c_s^{\alpha_c}$	(8)	–
Tafel equation	$j_{\text{para}}(x) = -j_{0,\text{para}}\times\exp\left(\frac{-\alpha_c F(\Phi_1(x)-\Phi_2(x)-U_{\text{para}}-Fij(x)R_f(x))}{RT}\right)$	(9)	–
Bruggeman relation	$D = D_e(\varepsilon(x))^{0.5}$	(10)	–
SEI thickness measurement	$\frac{\partial\delta_f(x)}{\partial t} = -\frac{j_{\text{para}}(x)\times M}{\rho_f\times F}$	(11)	$\delta_f = \delta_{0,f}$ at $t=0$
Film resistance measurment	$R_f(x) = \frac{\delta_f(x)}{k_f} + R_0$	(12)	–
Average change of the anode lithium stoichiometry	$\delta CSX = \frac{\int_0^{L_a} j_{\text{para}}(x)a(x)dx}{c_s(1-\varepsilon-\varepsilon_{fl})L_a}\delta t$	(13)	–

Table 2
Model properties and base case parameters.

Parameter	Unit	Explanation	Cathode	Membrane	Anode	Refs.
L_a, L_s, L_c	m	Thickness of domain	7.4×10^{-5}	2.5×10^{-5}	7.5×10^{-5}	[13]
α_a, α_c	–	Symmetry coefficient	0.5	–	0.5	[1]
i_0'	$m^{2.5}\,mol^{-0.5}\,s^{-1}$	Exchange current density	3×10^{-6}	–	10^{-6}	Assumed
$c_{0,e}$	$mol\,m^{-3}$	Initial concentration of electrolyte	1000	1000	1000	[1]
D_s	$m^2\,s^{-1}$	Intercalated diffusion coefficient	1.0×10^{-13}	–	3.8×10^{-14}	[13]
D_e	$m^2\,s^{-1}$	Diffusion coefficient of electrolyte	2.5×10^{-10}	2.5×10^{-10}	2.5×10^{-10}	[13]
$R_{s,a}, R_{s,c}$	m	Radius of electrode active particles	2.0×10^{-6}	–	2.0×10^{-6}	[13]
σ_s	$S\,m^{-1}$	Solid conductivity	10	0	100	[13]
C_t	$mAh\,g^{-1}$	Maximum concentration of Li in the solid phase	274	–	372	Dualfoil 5.1 code
ε	–	Volume fraction of electrolyte in electrode	0.338	0.37	0.44	[13]
ε_{fl}	–	Volume fraction of filler materials	0.142	–	0.07	[13]
t_0^+	–	Positive ion transfer number	0.2	0.2	0.2	[13]
M	$kg\,mol^{-1}$	Molecular weight			0.1	[13]
$R_{f,0}$	$\Omega\,m^2$	Initial film resistance	–	–	8.7×10^{-3}	[13]
k_f	$S\,m^{-1}$	SEI film conductivity	–	–	3.79×10^{-7}	[13]
$j_{0,para}$	$A\,m^{-2}$	Parasitic rate constant	–	–	8×10^{-8}	[13]
U_{para}	V	Parasitic equilibrium potential	–	–	0.38	[13]
ρ_f	$g\,m^{-2}$	Film density	–	–	2100	[13]

5. Numerical solution method

The present study uses Dualfoil 5.1 code, which has been developed for the simulation of the behavior of lithium and lithium ion cells [4]. It solves six coupled, nonlinear equations to calculate the potential in the electrode and electrolyte Φ_1 and Φ_2, the concentration of lithium ions in the electrodes and electrolyte c_s and c_e, and the interfacial and ionic current density j and i_2 as functions of time and position within the cell. Thomas algorithm has been used to take advantage of the tri-diagonal coefficient matrix [4]. In order to improve solution efficiency, Duhamel's superposition integral has been used to solve the Li diffusion equation in the solid phase [1]. So the problem will be simplified to a one dimensional system by removing the radial direction. The Crank–Nicolson implicit method is used to discretize the time derivatives.

The original computer code assumes constant values for porosity, specific interfacial area, radius of active particles, solid electrolyte interface thickness, and resistance across electrodes. We have modified the computer code to accommodate the variation of these parameters across the electrodes. Updating of SEI thickness and resistance is performed in each node at the end of each time step whereas lithium stoichiometry is updated at the end of cycles. In this way, it is possible to simulate easily large cycling numbers.

6. Model capability of charge and discharge simulation

As first step for the validation of the modeling method, the simulation results are compared with experimental data of Ref. [13]. In the present study we approximate the open circuit potential functions for anode and cathode based on the stoichiometry of lithium in electrodes using experimental data (Figs. 12 and 13 in Ref. [13]) and artificial neural network method which is a powerful nonlinear general approximator. So for the cathode the variation of the open circuit potential may be expressed as:

$$\begin{aligned} U_{Li_yCoO_2} = {} & 4.2111 + 0.35555(-1.197 + 0.023858\tanh[13.6643 \\ & -20.3126(1 + 4.03388(-0.9994 + y))] \\ & +0.79368\tanh[11.0714 - 11.4298(1 \\ & +4.03388(-0.9994 + y))] - 0.27105\tanh[1.3768 \\ & +2.7566(1 + 4.03388(-0.9994 + y))] - 0.050766\tanh \\ & [0.033872 + 4.5978(1 + 4.03388(-.9994 + y))] \\ & -0.10209\tanh[12.1061 + 12.2216(1 + 4.03388 \\ & (-0.9994 + y))] - 0.078158\tanh[15.1569 + 19.2125 \\ & (1 + 4.03388(-0.9994 + y))] \end{aligned} \quad (15)$$

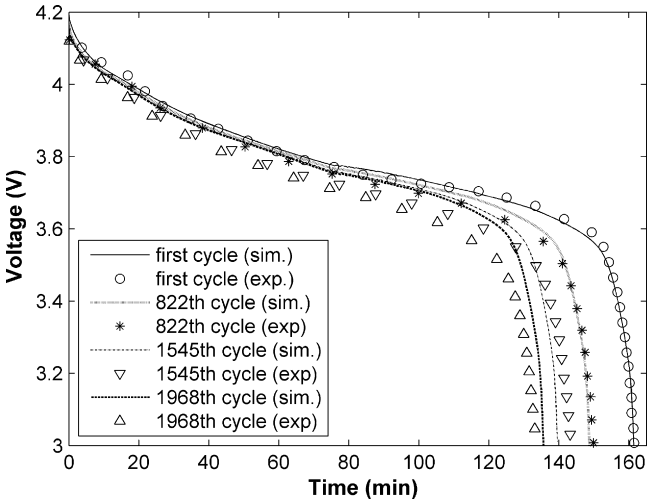

Fig. 4. Experimental [13] and simulated discharge curves at different cycle numbers.

And for the anode:

$$\begin{aligned} U_{MCMB} = {} & 1.183 + 0.57445(1.127 + 0.057472\tanh[7.8821 \\ & -7.5267(1 + 2.44978(-0.8154 + x))] \\ & +0.011615\tanh[5.5921 - 7.0027(1 \\ & +2.44978(-0.8154 + x))] + 0.034248\tanh[0.61451 \\ & -6.8326(1 + 2.44978(-0.8154 + x))] \\ & -0.084375\tanh[3.6351 + 5.475(1 \\ & +2.44978(-0.8154 + x))] - 0.47827\tanh[13.8605 \\ & +14.4346(1 + 2.44978(-0.8154 + x))] \\ & -2.5394\tanh[70.7177 + 69.9623(1 \\ & +2.44978(-0.8154 + x))]) \end{aligned} \quad (16)$$

where x and y are the stoichiometry of lithium in the negative and positive electrodes.

As mentioned in Section 4, in the present work, ionic conductivity is considered a function of electrolyte concentration, whereas in Ref. [13] it is assumed to be constant. Moreover, it seems that

Table 3
Detail explanation of different conditions in Figs. 6–11.

Condition label	Changed parameter respect to reference condition	Value of changed parameter respect to reference values listed in Table 2
Ref.	–	–
D_1	Electrolyte diffusion	$0.25D_e$
D_2	Electrolyte diffusion	$4D_e$
k_1	Ionic conductivity of electrolyte	$0.5k_e$
k_2	Ionic conductivity of electrolyte	$2k_e$
$a(x)$	Anode interfacial surface area	$0.7a + 0.6a(x/L_a)$
$\varepsilon(x)$	Anode porosity	$0.8\varepsilon + 0.4\varepsilon(x/L_a)$
$r(x)$	Anode active particle radius	$0.7R_a + 0.6R_a(x/L_a)$

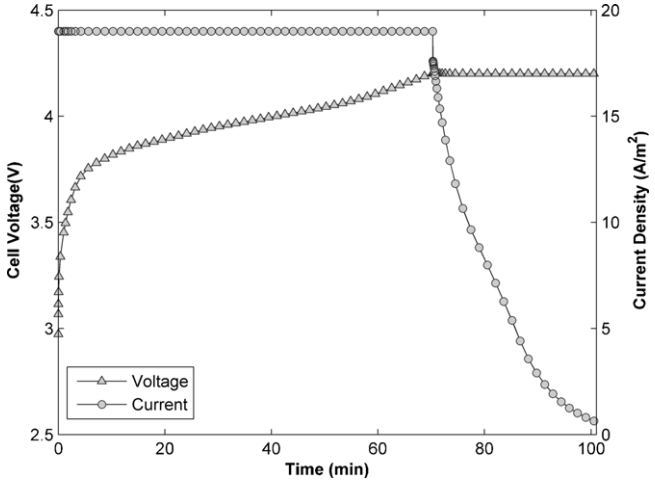

Fig. 5. Simulation of current density and voltage during first charge process.

in Ref. [13] consumption of lithium due to parasitic reaction have been accounted for twice during simulation of one cycle (once in Eq. (3) and another in Eq. (15) as a source term). In our work, we have modified the electrode concentration only at the end of cycles and did not insert it as a source term in the material balance equation.

As it is shown in Fig. 4, there is a good agreement between the measured discharge and our predicted results. Considering the very high complexity of the numerical model, the accuracy of the validation results is sufficient for further model analysis. The deviation of our predictions with the experimental data may be attributed to further aging mechanisms which are not considered in the model and is subject to further studies.

Fig. 5 shows the charge simulation capability of the model in its current form. The charge mode is divided into two different parts: CC and CV. At the CC, the battery voltage increases from 3 V to 4.2 V where charging state switches from galvanostatic (CC) to potentiostatic (CV). In this mode voltage is constant and current drops. When the charge current reaches 50 mA the charging process is stopped. The energy stored in the battery is calculated from current, voltage and time. About 13 percent of the energy is gained in the CV region of the charge process.

7. Result and discussion

7.1. Effect of different parameters on the variation across anode electrode

Numerical experiments have been performed to study the effects of different parameters on the variation of SEI layer, film resistance and parasitic side reaction across the thickness of the anode electrode. Studied parameters include the electrolyte properties: Li-diffusion and ionic conductivity, and the *variations* in the morphological characteristics: porosity, interfacial surface area and active particle radius across anode electrode. Table 3 shows the conditions prevailing in the parametric study. Moreover, the simulation results of the previous section are chosen as the reference condition.

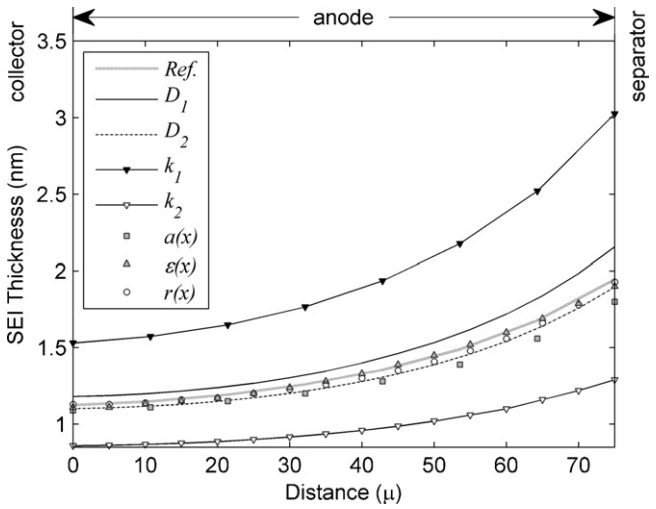

Fig. 6. Variation of SEI thickness across electrode for different conditions after 1900 cycles.

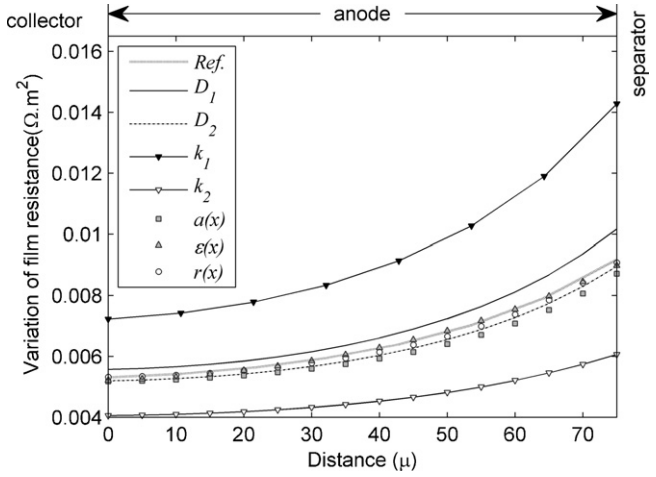

Fig. 7. Variation of film resistance across electrode for different conditions after 1900 cycles.

Figs. 6 and 7, respectively, show the variation of SEI thickness and film resistance across anode electrode corresponding to conditions of Table 3. From these figures, it is clear that:

1. For all cases, the SEI thickness and resistance film across anode electrode increase from the current collector side to the separator side. For example for the reference case, the SEI film thickness after 1900 cycles at anode/separator interface ($B_{2,3}$) is predicted to be 1.95 nm corresponding to variation in film resistance of $9.2 \times 10^{-3}\ \Omega\,m^2$ while at anode/collector interface ($B_{1,2}$) is predicted to be 1.13 nm corresponding to variation in film resistance of $5.3 \times 10^{-3}\ \Omega\,m^2$.
2. The ionic conductivity is more important with respect to SEI layer formation compared to other listed parameters in Table 3. Doubling the value of ionic conductivity would lead to a SEI layer thickness of 1.29 nm at anode/separator interface ($B_{2,3}$) and

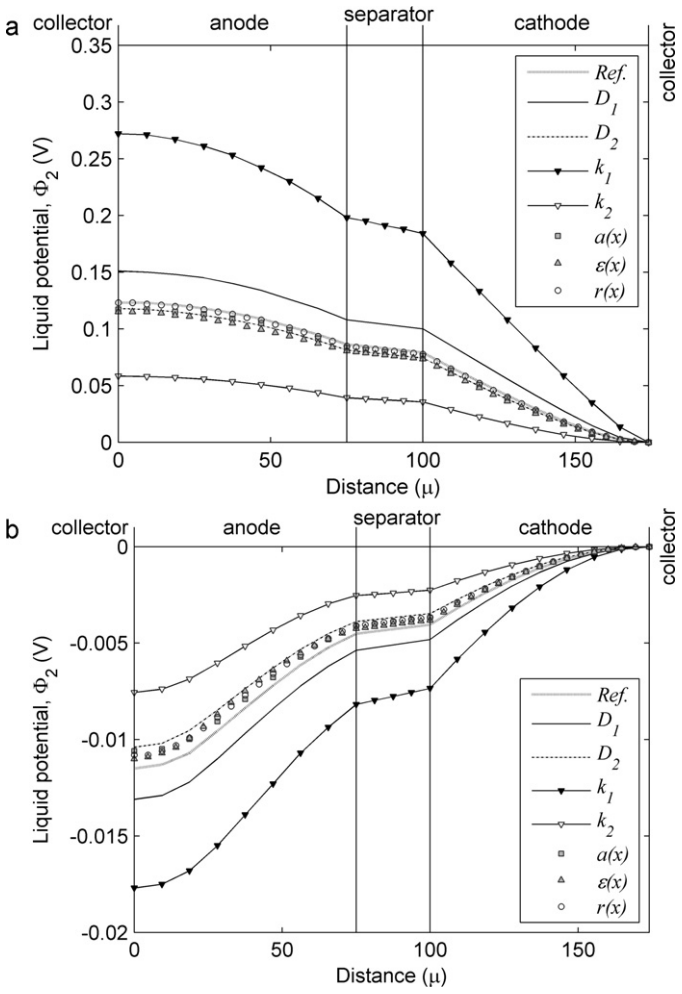

Fig. 8. Electrolyte potential across electrode at the first cycle (a) at the end of discharge and (b) at the end of charge.

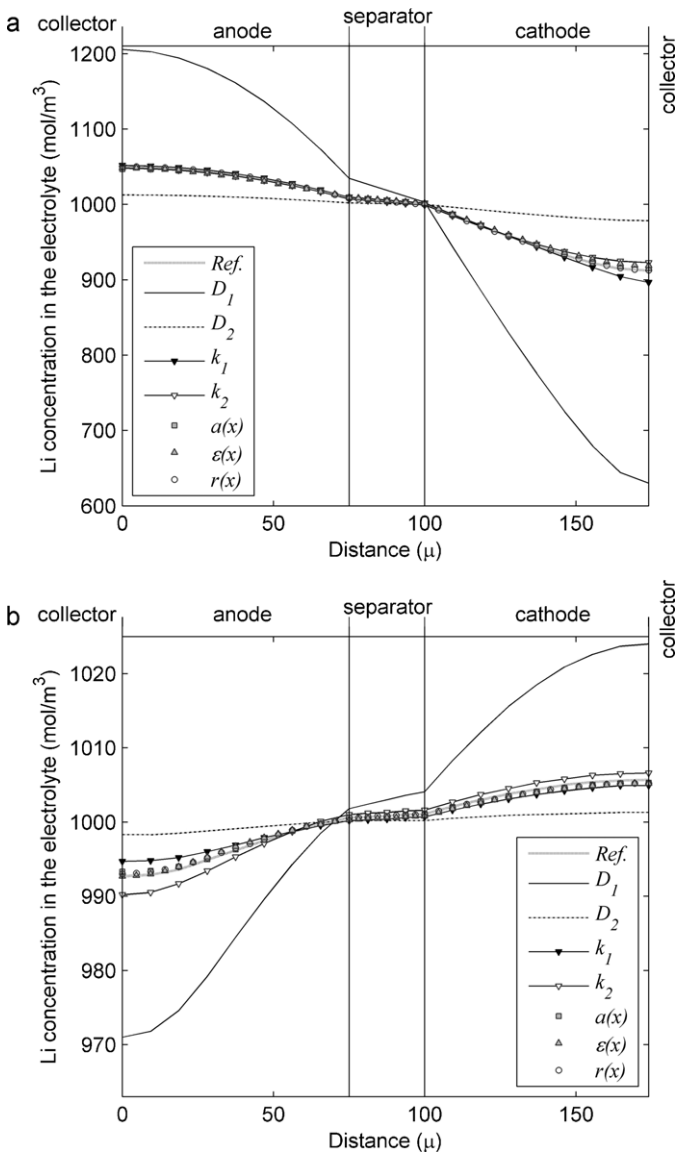

Fig. 9. Electrolyte concentration across electrode at the first cycle (a) at the end of discharge and (b) at the end of charge.

0.86 nm at anode/collector interface ($B_{1,2}$) so nonuniformity in SEI thickness reduces from 0.82 nm corresponding to the reference condition to 0.43 nm corresponding to a high value for the ionic conductivity.

3. The results for two different electrolyte diffusions and the reference conditions in Figs. 6 and 7 show that an increase in the electrolyte diffusion improves uniformity but the extent of this improvement decreases with increasing diffusion. This is because of diminishing changes in c_e gradient across electrodes for large diffusion values. This will be explained in more details in the next section.
4. Changes in the morphological parameters such as porosity, particle radius and surface area have minor effects on the SEI layer and film resistance.

To further clarify the mechanism of influence of different parameters in Table 3, variations of parasitic pore wall flux, solid and liquid potential and electrolyte concentration across anode electrode have been compared for different conditions in Table 3

7.1.1. Effect of electrolyte properties

As it is clear from Eq. (9), parasitic side reaction is a function of electric potential in the solid phase, Φ_1, in the liquid electrolyte phase, Φ_2, and the pore wall flux of lithium ions, j. Similarly, based on Eq. (7), j is also a function of electrode and electrolyte potential Φ_1 and Φ_2. The variation of solid potential Φ_1 across electrode is of the order of 10^{-5} V, whereas the variation of liquid potential Φ_2 is at least of the order of 10^{-2} V (Fig. 8) which is much higher than the solid potential. Therefore, in order to control the uniformity of reaction and reduce its intensity at the interface of anode and separator, it is necessary to control the electrolyte potential. Fig. 8 shows that ionic conductivity of electrolyte, k_e, has a dominant role on the potential in the electrolyte. This is explained by Eq. (4), the Ohm's law in electrolyte, which relates the electrolyte potential to the gradient of concentration logarithm and ionic conductivity of electrolyte.

Based on the data in Table 2, the first term in right hand side of Eq. (4) is more than one order of magnitude higher than the second term. Therefore adjusting the first term is more effective for controlling the liquid potential. Because k_e is directly appeared in this term, its variation has a significant effect on the first term. Consequently, k_e is expected to strongly influence the liquid potential. There have been some studies for improving electrolyte ionic conductivity, for example: synthesizing electrolytes with capability of holding large volumes of liquid component [27], adding additives to electrolyte [28], improving the particle network specially [29] and exposing polymers to gamma irradiation [30]. Normally, the main motivation for improving ionic conductivity is to decrease

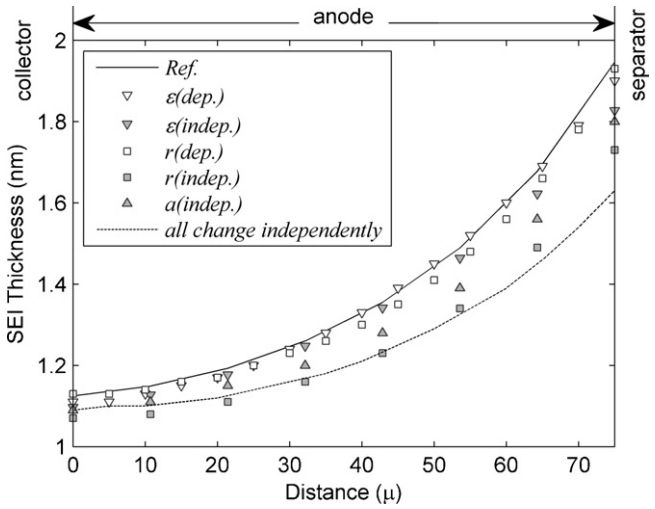

Fig. 10. the effect of gradient in interfacial surface area, porosity and radius on the SEI layer for dependent and independent conditions.

charge/discharge time. The present results show that aging of the electrodes is directly related to electrolyte conductivity and can be reduced by increasing the conductivity of the electrolyte.

The following points are relevant for the current modeling:

1. The electrolyte diffusion coefficient, D_e, does not appear explicitly in Eq. (4) and only affects electrolyte potential indirectly by adjusting electrolyte concentration.
2. The electrolyte concentration, c_e, appears in Eq. (4) inside the derivative of logarithm function. It is easy to verify that the variation of logarithm function is less than the variation of linear function when c_e is larger than one.
3. The range of variation of c_e is less than one order of magnitude (Fig. 9), Consequently, the effect of D_e is expected to be less important than the effect of k_e.

Fig. 9 shows that when the Li diffusivity, D_e, is one fourth of the reference condition (D_1), the gradient of c_e is much higher than that of the reference condition. However, the Li concentration gradient, c_e, is much lower when the electrolyte diffusion coefficient is four times bigger than the reference condition (D_2). Therefore, the c_e gradient has a *limited influence* which has been correctly predicted in Figs. 6 and 7, where an increase in the electrolyte diffusion initially improves uniformity but its effect diminishes for large values of diffusion coefficient. (SEI thickness over the anode/separator interface is 0.209 nm higher with respect to the reference value when diffusion is low while it is only 0.049 nm less than reference condition when diffusion is high.)

7.1.2. Effect of the morphological properties

In the present computer code, the interfacial surface area, a, in the electrode is calculated based on the assumption that all active particles are smooth spheres and are in contact with the electrolyte molecules. So if there are n particles per unit volume of the electrode, the interfacial surface area is equal to

$$a = 4n\pi R_a^2 \tag{17}$$

where R_a is the active particle radius in the electrode. n is calculated by considering the volumes of each components inside the electrode; the volume fraction of active particles is equal to $4/3n\pi Ra^3$. Moreover, ε and ε_{fl} are the volume fractions of the electrolyte and

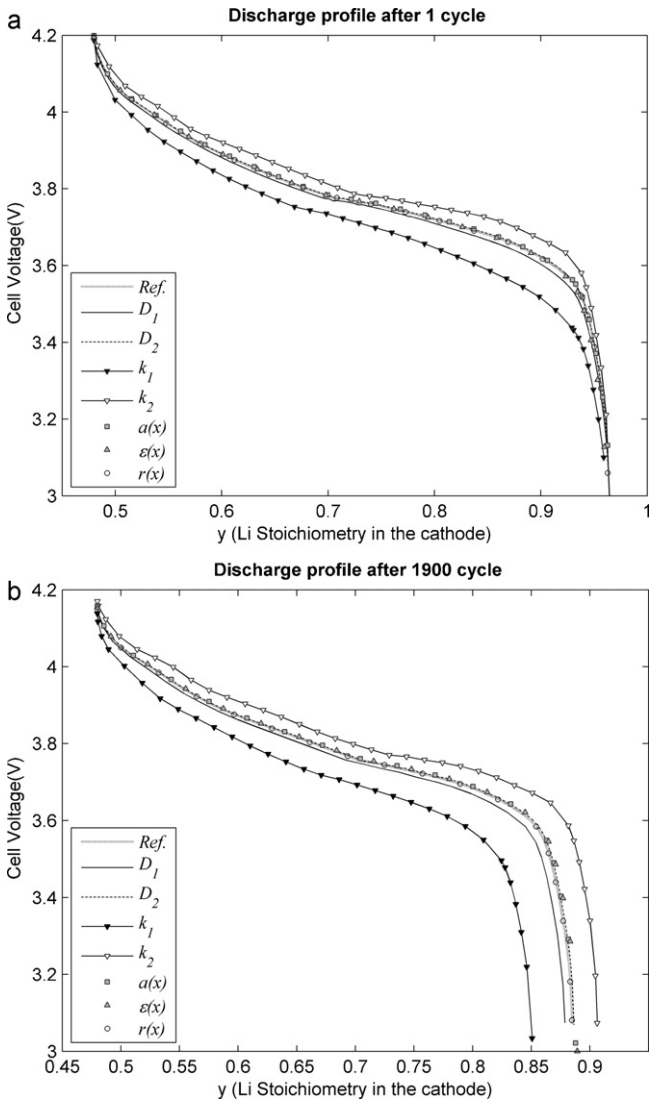

Fig. 11. Cell voltage profile in (a) first and (b) 1900th discharge cycle for different conditions.

fillers in the electrode, respectively. Therefore, their sum constitutes the whole volume:

$$\varepsilon + \varepsilon_{fl} + \frac{4}{3}n\pi R_a^3 = 1 \tag{18}$$

From Eqs. (17) and (18) the interfacial surface area is derived as [26]:

$$a = \frac{3(1-\varepsilon-\varepsilon_{fl})}{R_a} \tag{19}$$

Based on this equation, an increase in the active particle radius leads to a decrease in the interfacial surface area. This would cause two opposite effects on the reaction rate: deceleration of the diffusing rate of ions in the solid phase due to larger active particle radius, and higher reaction rates for supplying the same amount of current due to reduction of interfacial surface area. Similar statement is true for increasing porosity. As it is clear from Eq. (10), an increase in porosity would increase the diffusion in electrolyte, which results in fast penetration of ions in the depth of electrode, but also decreases the interfacial surface area. Therefore, change in the radius and porosity across electrode is concluded to have little effects on the uniformity of the reaction rate across electrode. Unlike porosity and radius of active particle, interfacial surface area could increase without

Table 4
CSX and *y* after 1900th cycle at the beginning and at the end of discharge mode for different conditions.

Condition	Ref.	k_2	k_1	D_2	D_1	$a(x)$	$\varepsilon(x)$	$r(x)$
CSX at the end of charge	0.6986	0.7345	0.6416	0.7011	0.6884	0.7022	0.7007	0.6982
y at the end of discharge	0.8847	0.9063	0.8508	0.8863	0.8786	0.8893	0.8847	0.8847

significant changes in porosity and radius. This could be done, for example, by growing nanofibers on the surface of graphite spheres [18]. Our results in Fig. 6 confirm that changes in the porosity, ε, and radius of active material in the anode electrode, R_a, have a minor effect on the uniformity of SEI layer across electrode.

Fig. 10 compares the effect of positive gradients of a, ε and R_a on the variation of SEI layer by changing each parameter dependently, when the variation of one parameter affects other(s) parameter(s) based on Eq. (19), as well as independently, when changing one of the parameters does not affect others. Result for the special case in which all three morphological parameters have positive gradient across anode electrode is shown in this figure. Comparing the results after 1900 cycling for the reference condition and the condition that all morphological parameters increase linearly across anode electrode shows that the thickness of SEI layer decrease from 1.95 nm in reference condition to 1.63 nm at anode/separator interface ($B_{2,3}$) and from 1.13 nm in reference condition to 1.09 nm at anode/collector interface ($B_{1,2}$). So non-uniformity decreases from 0.82 nm to 0.54 nm. It is clear that in this case changes significantly affect the uniformity. This could be used as a criterion in choosing new morphologies for the part of anode electrode connected to separator. It is predicted that using morphologies which have larger values of a, ε and r for this part of anode electrode improve the lifetime of the Li ion battery.

7.2. Performance of battery after large number of cycling

The profiles of cell voltage during discharge after the first and the 1900th cycle corresponding to different conditions are shown in Fig. 11(a) and (b). From Fig. 11(a) it is clear that the average voltage and the performance of battery increase by increasing the ionic conductivity. Morphological changes, including a, ε and r variations, have a minor effect when they are dependent to each other. Inhibition of the influence of the diffusion coefficient for large values of this parameter appears also in this figure. These results are in good agreement with the previous prediction results depicted in Figs. 6 and 7.

Fig. 11(b) shows that changes in the average cathode stoichiometry, y, at the end of discharge and aging of the battery follow a similar trend. There is a good consistency between this figure and Table 4 which shows average value of the lithium stoichiometry in the anode, *CSX*, at the beginning of discharge mode and y at the end of discharge mode after the 1900th cycle at for different conditions. Here we only updated *CSX* at the end of charge modes. So y variation at the end of discharge is an indirect result of lithium consumption in the anode electrode.

8. Conclusion

Detailed investigation of the morphological features of the anode and electrolyte properties provides the basis for improved lithium ion battery models. The present model further develops the computational capabilities of Dualfoil 5.1 code. New features of the proposed model provide possibility of studying variations in SEI layer thickness and resistance across the depth of anode electrode of lithium ion battery during large numbers of cycling. Moreover, the effects of variation of morphological parameters including porosity, specific interfacial area and radius of active particles across anode electrode on the uniformity of SEI layer are studied.

The thickness of SEI layer across electrode is a criterion for the intensity of critical condition across electrode. Based on the simulation results, the side of anode electrode connected to the separator experiences the worst conditions, which means high SEI thickness and film resistance. For example, the SEI film thickness after 1900 cycles at anode/separator interface ($B_{2,3}$) is predicted to be 1.95 nm corresponding to variation in film resistance of $9.2 \times 10^{-3}\ \Omega\,m^2$ while at anode/collector interface ($B_{1,2}$) is predicted to be 1.13 nm corresponding to variation in film resistance of $5.3 \times 10^{-3}\ \Omega\,m^2$. This non-uniformity of the SEI thickness and film resistance is mostly sensitive to ionic conductivity of electrolyte. Increasing this parameter is predicted to improve lifetime and performance of battery. Doubling the value of ionic conductivity would lead to a SEI layer thickness of 1.29 nm at anode/separator interface ($B_{2,3}$) and 0.86 nm at anode/collector interface ($B_{1,2}$) so non-uniformity in SEI thickness reduces from 0.82 nm corresponding to the reference condition to 0.43 nm corresponding to a high value for the ionic conductivity.

Increasing electrolyte diffusion from small values improves uniformity but the intensity of improvement decreases for large values of this parameter. SEI thickness over the anode/separator interface is 0.209 nm higher than the reference value when diffusion is one forth of reference condition, whereas it is only 0.049 nm less than the reference SEI thickness when diffusion is four time higher than the corresponding reference condition. The reason is that the electrolyte concentration gradient does not change significantly when diffusion coefficient is high.

Results also show that for assumption that all active particles are smooth spheres and are in contact with the electrolyte molecules, changes in the active particle radius and porosity across anode electrode lead to variations in interfacial surface area and the final result is concluded to have little effects on the uniformity of the reaction rate across electrode. However, when this limitation is relaxed and all these parameters could change independently, linear increase of all of them at the same time across anode electrode have considerable positive effects on the uniformity of side reaction. Comparing the results after 1900 cycling for the reference condition and the condition that all morphological parameters increase linearly across anode electrode shows that the thickness of SEI layer decrease from 1.95 nm in reference condition to 1.63 nm at anode/separator interface ($B_{2,3}$) and from 1.13 nm in reference condition to 1.09 nm at anode/collector interface ($B_{1,2}$). So non-uniformity decreases from 0.82 nm to 0.54 nm. This could be a criterion in choosing new morphologies for the part of anode electrode connected to separator.

Acknowledgments

Authors wish to thank Professor Newman and Dr. Albertus for their kind advises about Dualfoil 5.1 computer code.

References

[1] M. Doyle, T.F. Fuller, J. Newman, Journal of the Electrochemical Society 140 (1993) 1526–1533.
[2] T.F. Fuller, M. Doyle, J. Newman, Journal of the Electrochemical Society 141 (1994) 1–10.

[3] J. Newman, K.E. Thomas, H. Hafezi, D.R. Wheeler, Journal of Power Sources 119-121 (2003) 838–843.
[4] J. Newman, K.E. Thomas-Alyea, Electrochemical Systems , John Wiley & Sons, 2004.
[5] R. Darling, J. Newman, Journal of the Electrochemical Society 145 (1998) 990–998.
[6] J. Christensen, J. Newman, Journal of the Electrochemical Society 151 (2004) A1977–A1988.
[7] J. Christensen, J. Newman, Journal of the Electrochemical Society 152 (2005) A818–A829.
[8] T. Yoshida, M. Takahashi, S. Morikawa, C. Ihara, H. Katsukawa, T. Shiratsuchi, J.-i. Yamaki, Journal of the Electrochemical Society 153 (2006) A576–A582.
[9] P. Ramadass, B. Haran, R. White, B.N. Popov, Journal of Power Sources 111 (2002) 210–220.
[10] P. Ramadass, B. Haran, P.M. Gomadam, R. White, B.N. Popov, Journal of the Electrochemical Society 151 (2004) A196–A203.
[11] P. Ramadass, B. Haran, R. White, B.N. Popov, Journal of Power Sources 123 (2003) 230–240.
[12] G. Ning, B. Haran, B.N. Popov, Journal of Power Sources 117 (2003) 160–169.
[13] G. Ning, R.E. White, B.N. Popov, Electrochimica Acta 51 (2006) 2012–2022.
[14] P. Albertus, J. Christensen, J. Newman, Journal of the Electrochemical Society 155 (2008) A48–A60.
[15] M. Broussely, P. Biensan, F. Bonhomme, P. Blanchard, S. Herreyre, K. Nechev, R.J. Staniewicz, Journal of Power Sources 146 (2005) 90–96.
[16] G. Sarre, P. Blanchard, M. Broussely, Journal of Power Sources 127 (2004) 65–71.
[17] R. Darling, J. Newman, Journal of the Electrochemical Society 144 (1997) 4201–4208.
[18] H.-L. Zhang, Y. Zhang, X.-G. Zhang, F. Li, C. Liu, J. Tan, H.-M. Cheng, Carbon 44 (2006) 2778–2784.
[19] A. Magasinski, P. Dixon, B. Hertzberg, A. Kvit, J. Ayala, G. Yushin, Nature Materials 9 (2010) 353–358.
[20] N.N. Sinha, C. Shivakumara, N. Munichandraiah, ACS Applied Materials & Interfaces 2 (2010) 2031–2038.
[21] J. Christensen, Journal of the Electrochemical Society 157 (2010) A366–A380.
[22] S.J. Harris, A. Timmons, D.R. Baker, C. Monroe, Chemical Physics Letters 485 (2010) 265–274.
[23] B. Markicevic, N. Djilali, Physics of Fluids 18 (2006) 033101–033113.
[24] H.J. Gores, J. Barthel, Journal of Solution Chemistry 9 (1980) 939–954.
[25] W. Du, A. Gupta, X. Zhang, A.M. Sastry, W. Shyy, International Journal of Heat and Mass Transfer 53 (2010) 3552–3561.
[26] M. Doyle, J. Newman, Electrochimica Acta 40 (1995) 2191–2196.
[27] D.M. Tigelaar, A.E. Palker, M.A.B. Meador, W.R. Bennett, Journal of the Electrochemical Society 155 (2008) A768–A774.
[28] H. Ye, J. Huang, J.J. Xu, A. Khalfan, S.G. Greenbaum, Journal of the Electrochemical Society 154 (2007) A1048–A1057.
[29] S.K. Das, A.J. Bhattacharyya, The Journal of Physical Chemistry C 113 (2009) 6699–6705.
[30] S. Tarafdar, S.K. De, S. Manna, U. De, P. Nanda, Pramana Journal of Physics 74 (2010) 271–279.